

Empirical formulas for near-bed wave orbital velocity parameters involved in maximum wave load in random wave trains

メタデータ	言語: English 出版者: 公開日: 2024-07-17 キーワード (Ja): キーワード (En): 作成者: 川俣, 茂, 小林, 学 メールアドレス: 所属: 水産研究・教育機構, 国際気象海洋株式会社
URL	https://fra.repo.nii.ac.jp/records/2009878

Empirical formulas for near-bed wave orbital velocity parameters involved in maximum wave load in random wave trains

Shigeru Kawamata^{a,1}, Manabu Kobayashi^b

^aKamisu Branch, Fisheries Technology Institute, Japan Fisheries Research and Education Agency, Hasaki, Kamisu, Ibaraki 314-0408, Japan

^bChoshi Branch, International Meteorological and Oceanographic Consultants Co. Ltd., Kawaguchicho, Choshi, Chiba 288-0001, Japan

* Corresponding author.

E-mail address: kawamata_shigeru76@fra.go.jp (S. Kawamata)

Abstract

This paper presents empirical methods utilizing recently developed formulas (Kawamata and Kobayashi., 2022; Kawamata et al., 2018) to predict the maximum wave forces on near-bed structures and wave-induced movement ratios of isolated rocks in random wave trains. The methods assume that the maximum wave load occurs when the velocity semi-amplitude defined as half the difference between successive negative and positive peaks of the near-bed wave orbital velocity is maximized. The empirical formulas for the velocity-waveform parameters at the maximum velocity semi-amplitude in a random wave train were derived from the near-bed velocities and surface elevations measured in laboratory wave flumes. The laboratory formula for the maximum velocity semi-amplitude was reviewed and improved with near-bed wave orbital velocities and surface elevations estimated from pressure measurements under a wider range of wave conditions in the field. The newly developed formulas for the velocity-waveform parameters at velocity semi-amplitude maxima, combined with the previously developed formulas, showed reasonable agreement with the maximum wave forces measured on the artificial reef models under random waves in a laboratory wave flume as well as with the movement ratio of quarry rocks (median mass = 0.40 t) observed in a field test.

Keywords: Wave orbital velocity; Maximum wave force; Rock movement; Random wave train

1. Introduction

The near-bed velocity waveform yielding the maximum wave load on a seabed object must be predicted to assess its stability in coastal water. As a practical approach, the maximum force has been assumed to occur under the maximum wave height in a random wave train. The velocity waveform based on the linear wave theory or nonlinear periodic wave theories such as Stokes fifth order wave theory has normally been used to assess the wave force by utilizing the Morison equation, which represents the time-varying force as the sum of the drag force proportional to the instantaneous velocity squared and the inertia force proportional to the acceleration of water (Sarpkaya and Isaacson, 1981; Sobey, 1990; Gudmestad, 1993; ISO 21650, 2007). In the surf zone, the complex wave orbital velocity enforces more simplifying assumptions, viz., (1) the inertia force is negligibly small in comparison to drag force and (2) the maximum horizontal velocity can be estimated from the height of a depth-limited breaking wave (e.g., Denny, 1995; Nott, 1997; Lorang, 2000). However, these assumptions are far from reality, and existing studies have neither demonstrated the occurrence of the maximum wave load at the maximum wave height nor validated such predictions.

A more fundamental question pertains to the characteristic properties of the ambient velocity toward the maximum hydrodynamic load in individual random waves. Thus far, the maximum wave force in a random wave train has been presumed to occur in a wave with the maximum peak onshore (defined here as “positive”) horizontal velocity. However, a recent experimental study (Kawamata and Kobayashi, 2022) demonstrated that the maximum hydrodynamic horizontal force in individual random waves is closely related to the velocity semi-amplitude (U_a), defined as half the difference between the successive negative (U_{p-}) and positive peak horizontal velocities (U_{p+}), i.e., $U_a = (U_{p+} - U_{p-})/2$, rather than to the maximum horizontal velocity (normally identical to U_{p+}). This finding assisted with the derivation of the following empirical formula for the maximum or peak horizontal wave force, F_p :

$$F_p = \frac{1}{2} \rho C_F A U_a^2, \quad (1)$$

where ρ is the mass density of water, C_F is the maximum force coefficient, and A is the reference area of the object. C_F is expressed as a function of the Keulegan–Carpenter (KC) number, which is defined as

$$K_C = \frac{2U_a T_{pp}}{D}, \quad (2)$$

where T_{pp} is the period between the negative and positive peak velocities and D is the reference width of the object. Eq. (1) can be used to predict the maximum force and is more precise than the Morison equation, even for the asymmetric orbital velocities of shoaling and breaking waves (Kawamata and Kobayashi, 2022). Furthermore, the highest maximum wave force ($F_{p,\max}$) in a random wave train can be reasonably predicted as (Kawamata and Kobayashi, 2022)

$$F_{p,\max} = \frac{1}{2} \rho C_F (K_C^*) A U_a^{*2} \quad (3)$$

with

$$K_C^* = \frac{2U_a^* T_{pp}^*}{D}, \quad (4)$$

where the asterisk indicates the value of the “maximum velocity waveform,” defined as the individual zero-down-crossing wave of the velocity-time profile with the maximum U_a in a random wave train.

An experimental study yielded a similar finding regarding the stability of isolated quarry rocks under waves or waves with currents (Kawamata et al., 2018); the study revealed that the stability is more closely related to the maximum value for the velocity semi-amplitude of zero-down-crossing waves than to the positive peak velocity. This finding caused the development of the following practical equations for predicting the probabilistic mobility of isolated quarry rocks on a relatively flat bed (Kawamata et al., 2018):

$$r_d = \exp\{-\exp[-0.608(\phi - 4.17)]\}, \quad (5)$$

with

$$\phi = \left(7.28 - \ln \frac{U_{p+}^* T_{zp}^*}{D_{n50}} \right) \frac{U_a^{*2}}{\mu_{50} \Delta g D_{n50}}, \quad (6)$$

where r_d is the probability of the “damage” or “significant move,” defined as the displacement of a rock completely away from the initial occupied area in a wave train (refer to Kawamata et al. (2018) for a detailed definition); T_{zp} is the period between the zero up-crossing and the immediately subsequent positive peak velocity; $D_{n50} = (M_{50}/\rho_s)^{1/3}$, with M_{50} and ρ_s denoting the median mass and mass density of the rocks, respectively; μ_{50} is the median friction coefficient between the rocks and bed, $\Delta = \rho_s/\rho - 1$; and g is the acceleration due to gravity. Despite the extremely complex near-bed orbital velocity in random waves, these new equations are simple and can perform predictions with reasonable precision.

The models based on the velocity semi-amplitude may differ markedly from the Morison equation and conventional wave force formulas based on the maximum peak velocity, particularly at shallow sites where the near-bed velocity profile is strongly skewed (i.e., U_{p+} is considerably larger than $|U_{p-}|$). For example, for a coastal rocky site where an asymmetric maximum velocity waveform with $U_{p+} = 3.5$ m/s, $U_{p-} = -1.5$ m/s, and $T_{zp} = 2.0$ s was observed, the new formula (Eq. (5)) reasonably explained the test result that only 2 out of 10 quarry rocks with an average mass of 2 Mg (or t) moved, while a conventional formula for calculating the minimum stable mass of rocks from the maximum velocity alone, yielded a predicted value of 46 t, differing considerably from the observed value (Kawamata et al. 2018).

Two practical approaches have been proposed to calculate the wave-induced velocity profile near the bed in random sea states: one is to calculate the root mean square velocity using a generic form of the parametric surface-wave spectrum from significant wave height and peak period (Soulsby, 1987; Wiberg and Sherwood, 2008), and the other is to calculate the velocity waveform using wave height, wave period, local water depth, and local bed slope (Dibajnia et al., 2001; Tajima and Madsen, 2002; Tajima, 2004; Elfrink et al., 2006). Both approaches have been used to assess wave energy dissipation and sediment transport, but none has been used to predict maximum wave load in random wave trains. As the viewpoint that the maximum wave load on seabed objects occurs at the maximum velocity waveform in a random wave train is new and unprecedented, a practical method to predict the characteristic properties of the maximum velocity waveform (U_a^* , T_{pp}^* , U_{p+}^* , and T_{zp}^*) has not yet been developed.

This paper presents empirical equations to predict the above velocity properties and develop the practical methods required to estimate the maximum horizontal wave force acting on seabed objects or the stability of rocks under random waves. Accordingly, accurate measurements of near-bed wave orbital velocities under shoaling random waves were recorded in the laboratory to develop reliable, empirical equations for the characteristic properties of the maximum velocity waveform. Moreover, field measurements of near-bed pressure and velocity were performed to review and improve the equations, because the actual wave orbital velocity could be more variable and its accurate determination could be challenging owing to the highly complex and turbid natural conditions. Ultimately, the prediction methods for the maximum wave force and rock stability in random waves were experimentally validated.

2. Laboratory measurements

Laboratory measurements of near-bed velocities under random waves were performed at the Kamisu Branch, Fisheries Technology Institute (formerly known as the National Research Institute of Fisheries Engineering), Kamisu, Ibaraki, Japan. As depicted in Fig. 1, two wave flumes were used: one with dimensions of 70 m (length) \times 0.7 m (width) \times 2.2 m (total depth) and a slope of 1:50, and the other with dimensions of 101 \times 1 \times 2 m and a slope of 1:30. The measurement cross-sections were set up at six uniformly spaced depths of 0.3–0.55 m on the slope in each wave flume. At each measurement cross-section, a Nortek Vectrino (Nortek, Norway) acoustic Doppler velocimeter with a four-beam down-looking probe and a capacitance-type wave gauge were set up to measure the horizontal velocity 4 cm above the bottom and the water surface elevation, respectively. In preliminary experiments, the velocities were measured 8 cm above the bottom as well. The resultant deviation in U_a^* measurements was negligible (ranging from -6% to 6.7% with an average of -0.4%), ensuring that the measured velocity was a nearly constant wave orbital velocity within the near-bed layer above the thin wave boundary layer. Random waves were generated based on the modified Bretschneider-Mitsuyasu spectrum

(Goda, 1988). Nine wave runs were performed with various combinations of incident wave heights and periods (Table 1) in each wave flume so that various shapes of nonbreaking, breaking, and broken waves would occur at the measurement depths. In each run, the velocities and surface elevations were recorded at 50 Hz for more than about 250 individual waves. Thus, 6 (depths) \times 9 (wave runs) \times 2 (slopes) = 108 sets of time-series data were obtained for analysis.

3. Field measurements

3.1. Measurement locations and methods

Field measurements of the near-bed velocity and pressure were conducted at three different locations—Shiwagi, Hiwasa, and Mashike (Fig. 2), on the rocky coasts of Japan—as listed in Table 2. The measurement locations and periods were selected to cover a broad range of hydrodynamic conditions.

Shiwagi and Hiwasa are located on the Pacific coast of Shikoku, southwestern Japan. Among the three locations, the measurement point off Shiwagi was the deepest (mean water depth: 9.3 m) and completely exposed to ocean swells. The measurements that were performed between July 29 and November 17, 2015 recorded huge swells generated by two simultaneous typhoons (typhoons 201511 and 201512; <http://agora.ex.nii.ac.jp/digital-typhoon/year/wnp/2015.html.en>). The measurements off Hiwasa, 8.7 km southwest of Shiwagi, were acquired at the shallowest depth (mean depth: 5.3 m) between November 22, 2018, and February 5, 2019, during which local wind-generated waves occurred occasionally. The average slopes of the seabed between 0 and 50 m offshore from the measurement location were 0.03 and 0.05 for Shiwagi and Hiwasa, respectively. At these two locations, wave gauges (model WH-501, IO Technic Co., Ltd., Tokyo) were used to measure the velocity and pressure at 2 Hz (Shiwagi) and 5 Hz (Hiwasa) for 20 min every hour. The wave gauges are essentially bottom-mounted pressure gauges and biaxial electromagnetic current meters (ECMs), referred to as PUV gauges. The pressure and velocity sensors were mounted 57 and 66 cm above the seabed, respectively.

Mashike is located on the Japan Sea coast of Hokkaido, northern Japan. Although the coastal waters are open to the west and are frequently subjected to high waves caused by the western seasonal winds during autumn and winter, they have a limited fetch (approximately 400–500 km from the west) that produces waves with periods shorter than those at the other two locations. The seabed slope surrounding the measurement point was most gentle (approximately 0.02). A wave gauge (model WH-503, IO Technic Co., Ltd., Tokyo) equipped with PUV gauges and an upward-looking ultrasonic wave gauge was placed at a mean water depth of 7.57 m to measure the velocity, pressure, and surface elevation at 2 Hz for 20 min every hour between October 9 and November 30, 2017. However, the velocity measurements were only performed until November 11, 2017, because the stainless-steel velocity sensor with a diameter of 15 mm was bent by some collision during a heavy wave and stopped functioning.

3.2. Data analysis

The surface wave elevation and consequent orbital velocity near the bottom were calculated using the pressure as follows: time-series pressure data were firstly quadratically detrended to eliminate the tidal motion and subsequently Fourier-transformed. The i -th Fourier component was converted into the corresponding components of elevation and velocity by multiplying the following factors, $K_{p\eta}(\omega_i)$ and $K_{pu}(\omega_i)$, respectively, based on the linear wave theory and under the assumption that the wave components with frequencies lower than $f_{\min} = 0.04$ Hz and higher than the deep-water wave limit are negligible:

$$K_{p\eta}(\omega_i) = \begin{cases} \frac{1}{\rho g} \frac{\cosh k_i h}{\cosh k_i z_p} & \text{for } 2\pi f_{\min} < \omega_i < \sqrt{\pi g/h} \\ 0 & \text{elsewhere} \end{cases} \quad (7)$$

and

$$K_{pu}(\omega_i) = K_{p\eta}(\omega_i) \omega_i \frac{\cosh k_i z_u}{\sinh k_i h}, \quad (8)$$

where $\omega_i = 2\pi f_i$ and $k_i = 2\pi/L_i$ (f_i : the frequency; L_i : the wavelength) are the angular frequency and wave number, respectively, for each Fourier component; z_p and z_u are the vertical distances from the seabed to the pressure and velocity sensors, respectively; and h is the burst-mean depth. The lower and upper cut-off frequencies were useful for attaining a stable energy period and removing the effect of noise, respectively. k_i is related to ω_i through the linear dispersion equation:

$$\omega_i^2 = g k_i \tanh k_i h. \quad (9)$$

The time-series of surface elevation and near-bed wave orbital velocity were produced using the inverse Fourier transform. The term $\cosh k_i z$ on the right-hand side of Eqs. (7) and (8) remained almost at unity (<1.013) for the field conditions of z_p or $z_u \leq 0.66$ m, $h > 3.9$ m, and in a major-wave frequency range ($\omega_i = 2\pi/T_i < 1.26$ rad/s or $T_i > 5$ s), implying that these pressure and velocity measurements can be regarded as near-bed values.

Although the surface elevations and near-bed wave orbital velocities were directly measured using an ultrasonic wave gauge and ECMs, respectively, these measurements were frequently missing or heavily contaminated with spikes at high wave heights. In this study, the pressure-estimated surface elevation and wave orbital velocity were validated by comparing the results with direct measurements (refer to Appendix A); then, these values were used as the most robust standard measures to assess or improve the prediction formulas whose derivations are provided below.

4. Development of empirical formulas

4.1. Formula for U_a^*

The formula developed for predicting U_a^* can be expressed as

$$U_a^* = \alpha U_{\text{Airy}} \quad (10)$$

with

$$U_{\text{Airy}} = \frac{\omega_s H_{\text{max}}}{2 \sinh k_s h}, \quad (11)$$

where α is a correction factor to be empirically determined; U_{Airy} is the reference velocity calculated from the linear wave theory as the near-bed orbital velocity amplitude due to the maximum wave height (H_{max}); and ω_s and k_s are the linear wave values for the significant wave period (T_s) defined by the zero down-crossing method. Although the peak wave period is generally used to represent the wave periods for random waves, T_s was used to calculate the wavelength (L) according to the linear wave theory, because the peak period was discontinuously variable with respect to time, whereas T_s was stable even for a bimodal wave spectrum.

The empirical formula for the correction factor α was derived from regression analysis between the ratio $\alpha \equiv U_a^*/U_{\text{Airy}}$ and possible dimensionless parameters of H_{max}/h , H_{max}/L , H_s/L , h/L , H_s/h , and $\sqrt{h/g}/T_s$, where H_s is the significant wave height defined by the zero down-crossing method. Regression analysis using a single explanatory variable based on the accurate laboratory data revealed that the correlation factor was the most closely related to H_{max}/h , and its laboratory model (α_{lab}) was obtained as the nonlinear least-squares regression equation (the standard error of the regression (SER) = 0.0477, the adjusted R-squared $R_{\text{adj}}^2 = 0.698$, and $n = 108$; Fig. 3):

$$\alpha_{\text{lab}} = 1 - 0.396 \tanh \left[1.39 \left(\frac{H_{\text{max}}}{h} \right)^{1.46} \right]. \quad (12)$$

The field data, excluding the low waves ($H_{m0} < 0.4$ m, where H_{m0} is the significant wave height defined as four times the standard deviation of the surface elevation) that could bear considerable wave reflections and were less significant, exhibited a similar relationship between H_{max}/h and U_a^*/U_{Airy} on average, but with a large scatter, as shown with colored symbols in Fig. 3. This scatter partially resulted from the error due to the estimation from pressure but could be accounted for by the parameters other than H_{max}/h .

The ratio of the wave height at the maximum velocity waveform, H^* , to the maximum wave height from the laboratory data is depicted in Fig. 4. Evidently, U_a^* occurred at the maximum or near-maximum wave height at deeper depths of $H_{\text{max}}/h < 0.4$; however, the wave height at the maximum velocity waveform decreased further from the maximum wave height as H_{max}/h increased. This finding implies that U_a^* in the water of finite depth was influenced by the entire wave spectrum or H_s , rather than by the extreme waves or H_{max} . Multiple linear regression analysis examining which parameter could best account for the unexplained variation $U_a^*/(\alpha_{\text{lab}} U_{\text{Airy}})$ consistently revealed that the most significant parameter was H_s/L but that H_{max}/L was least significant (Table 3). Considering a wider range of wave conditions of the field data as well as a significant dependence of α on H_s/L , a prediction equation for the correction factor was

reconstructed by fitting the field data as a nonlinear regression model of α (SER = 0.0509, $R_{\text{adj}}^2 = 0.490$, and $n = 4005$):

$$\alpha_{\text{field}} = \left\{ 1 - 0.471 \tanh \left[1.46 \left(\frac{H_{\text{max}}}{h} \right)^{1.44} \right] \right\} \left(0.947 + 3.77 \frac{H_s}{L} \right). \quad (13)$$

The values of U_a^* predicted using Eqs. (12) and (13) based on the measured values of H_{max} , H_s , and T_s , were compared to the laboratory measurements or field pressure-estimated values (Fig. 5). The field model shown in Eq. (13) slightly improved the predictions, and its relative errors were almost within $\pm 10\%$ for both the field and laboratory data.

4.2. Formula for T_{pp}^*

The formula for T_{pp}^* was obtained by seeking the dimensionless parameter that could best account for the variations in the ratio $r_{pp} \equiv 2T_{pp}^*/T_s$ observed in the laboratory. Consequently, the Ursel number, $U_r = H_{\text{max}}L^2/h^3$, was found the most explanatory variable for r_{pp} , but it had scatter values much higher than one (Fig. 6), which was not expected from the asymmetric wave orbital velocity profiles in finite-depth water. As illustrated in Fig. 7, the maximum velocity waveforms with larger r_{pp} values did not exhibit sharp increases (thus had lower accelerations) between the negative and positive peaks. The accurate prediction of such fluctuations is challenging. For practical use in predicting maximum wave forces, however, because the wave forces are smaller for larger T_{pp} , the following equation for T_{pp}^* was derived as a conservative value from a nonlinear least-squares regression analysis based on the data excluding outliers with unexpectedly high r_{pp} (Fig. 6):

$$r_{pp} \equiv \frac{2T_{pp}^*}{T_s} = \min\{1, 0.515[1 + \exp(-0.00939U_r)]\}. \quad (14)$$

4.3. Formula for U_{p+}^* and T_{zp}^*

Unlike U_a^* , the variations in U_{p+}^* and T_{zp}^* could not be fully predicted, because both parameters are one-sided extreme variables, which are more prone to fluctuations due to the phase of low-frequency wave components than U_a^* , which is a two-sided extreme variable. However, these parameters are of secondary importance and appear only in the multiplicative form of $U_{p+}^*T_{zp}^*$ in Eq. (6). Thus, the best single-variable model for the ratio $r_{zp} \equiv 4U_{p+}^*T_{zp}^*/(U_{\text{Airy}}T_s)$ was searched for and r_{zp} was found to be the most closely correlated to H_{max}/h , but with large outliers (Fig. 8). According to Eqs. (5) and (6), r_d increases with decreasing $U_{p+}^*T_{zp}^*$, so the following model (denoted using a line in Fig. 8) fitting to the lower data points was adopted as a conservative threshold of rock stability:

$$r_{zp} \equiv \frac{4U_{p+}^*T_{zp}^*}{U_{\text{Airy}}T_s} = 1 - 0.967 \tanh \left[0.855 \left(\frac{H_{\text{max}}}{h} \right)^{0.883} \right]. \quad (15)$$

5. Validation of methods in terms of maximum wave forces and rock stability

5.1. Maximum wave forces in laboratory

Existing laboratory data (Kawamata and Kobayashi, 2022) describing the wave forces acting on three differently shaped structures (artificial reef models) placed on the bed were used to examine the accuracy of Eq. (3) according to the formulas proposed for U_a^* and T_{pp}^* (i.e., Eqs. (13) and (14)), which can predict the maximum horizontal wave force using the random wave properties H_{\max} , H_s , and T_s . Specifically, C_F for each structure was determined using an empirical function of the KC number based on regular wave tests, and the $F_{p,\max}$ predictions were consistent with the measurements; almost all errors were within $\pm 20\%$ (Fig. 9).

5.2. Rock stability in field

To validate Eqs. (5) and (6) to predict the probability of the mobility of isolated rocks under waves, a field experiment was conducted with quarry rocks on a relatively flat boulder site near the velocity measurement location off Mashike. In total, 10 quarry rocks (R1–R10) with similar masses of 0.37–0.43 t and $M_{50} = 0.40$ t were selected. Each rock was placed on the ground with its maximum surface area oriented downward, and a U-bolt composed of a reinforced steel bar was embedded and attached to the top surface of the rock using chemical anchors. The quarry rocks were placed on the test site by suspending them from the U-bolt in intervals of approximately 2 m on August 29, 2017 (Fig. 10). Significant moves of angular stones would generally involve overturning, as observed in the laboratory (Kawamata et al., 2018). Therefore, to determine the instant at which the rocks moved significantly, their inclinations were monitored using 10 accelerometers (MSR 145, MSR Electronics GmbH, Switzerland). Each accelerometer was encapsulated in a waterproof case, covered by a stainless-steel cylindrical container, and attached to the U-bolt on the quarry rock to record the three-axis accelerations at 1 min intervals. The measurements were conducted during the time period of the pressure measurement shown in Table 2. If the quarry rock overturned, the relative direction of the gravitational acceleration in the xyz -coordinates of the accelerometer changed considerably. Thus, the change in the relative direction could be obtained using

$$\gamma = \arccos \frac{a_x(0)a_x(t) + a_y(0)a_y(t) + a_z(0)a_z(t)}{\sqrt{a_x^2(0) + a_y^2(0) + a_z^2(0)} \sqrt{a_x^2(t) + a_y^2(t) + a_z^2(t)}}, \quad (16)$$

where $(a_x(0), a_y(0), a_z(0))$ and $(a_x(t), a_y(t), a_z(t))$ denote the triaxial acceleration components recorded at the initial time ($t=0$) and at time t , respectively, and γ is the angle between these two vectors. Note that the accelerometers were not specifically oriented with respect to the direction of gravity owing to difficulty in adjusting their mounting orientations.

A quarry rock was regarded as moving or rolling when the deviation between the triaxial vector magnitude of acceleration $\sqrt{a_x^2 + a_y^2 + a_z^2}$ and 1 G (where 1 G = 9.80665 m/s²) was larger than the threshold value set as 0.05 G; otherwise, it was deemed to be still. For convenience, a “still” quarry rock was assumed to have overturned (thus significantly moved) when $\gamma > 45^\circ$. However,

significant moves cannot be detected based on γ alone because quarry rocks can return with respect to the relative direction after rolling. Therefore, the time at which the sum of the changes in the following two angles was greater than 45° was used as an additional criterion for detecting significant moves: (1) the angle between the triaxial acceleration vector and z -axis and (2) the angle between x -axis and the vector projected onto the xy -plane.

To calculate r_d using Eqs. (5) and (6), μ_{50} was determined using the following empirical formula (Kawamata et al., 2018):

$$\mu_{50} = \tan \theta_{50} \quad (17)$$

with

$$\theta_{50} = 32.5 + 10.8 \exp\left(-0.23 \frac{D_{n50}}{B_{50}}\right), \quad (18)$$

where θ_{50} is the median friction angle in degrees and B_{50} is the median surface grain size of the seabed. Based on photographic images of the seabed, B_{50} of the experimental site was determined to be 0.238 m ($n = 232$) as the area-weighted average of the short-axis diameters of the surface grains. The r_d prediction at time t was obtained as the maximum of the r_d values calculated for burst data up to time t .

Fig. 11 shows the temporal variations in H_{\max} and the observed versus predicted r_d values of the test quarry rocks. The small sample size ($n = 10$) was responsible for a large deviation between the upper and lower 95%-confidence limits for true r_d , which were estimated based on binomial distribution. Despite the large time variation in the wave height, the predictions exhibited good overall agreement with the observations (Fig. 11).

6. Discussion and conclusions

Eqs. (10), (11), and (13)–(15) are the formulas for the characteristic properties of the maximum velocity waveform (i.e., U_a^* , T_{pp}^* , and $U_{p+T_{zp}}^*$), enabling Eqs. (3) and (5) to be used to predict the maximum wave force on near-bed structures and the wave-induced instability of rocks, respectively, in random wave trains. The assumption that the maximum wave force in random wave trains occurs at the maximum velocity semi-amplitude rather than at the maximum wave height is practically valid, even in the surf zone. Although large flow accelerations in the maximum velocity waveform could have always resulted in small T_{pp}^* or T_{zp}^* values, wave irregularity could produce unexpectedly large T_{pp}^* or $U_{p+T_{zp}}^*$ values, suggesting that the maximum wave force can occur in velocity waveforms with the second or third largest U_a value and smaller T_{pp} or T_{zp} values. However, it is challenging to derive the equations for the joint prediction of these parameters that will cause the highest maximum wave force. Therefore, for simplicity, the equations were modified only for T_{pp}^* and $U_{p+T_{zp}}^*$ by removing the unexpectedly large values as outliers to ensure that the collective proposed formulas yield conservative force

predictions. Nevertheless, the developed formulas for the maximum wave forces and wave-induced instability of rocks demonstrated good agreement with the observations.

The formulas relating the velocity parameters required to predict the maximum wave load in random wave trains use H_{\max} as a reference wave height, although the maximum velocity waveform mostly occurs at wave heights lower than H_{\max} in water of finite depth. The largest value of U_a in a wave train undoubtedly depends on the length of the wave record, as does the value of H_{\max} . In this study, the measurement duration did not cover more than number of waves sufficient to determine the maximum wave (normally, more than 250 waves) in all cases; thus, the observed maximum velocity waveforms may have been underestimated for longer wave trains. Nonetheless, the problem may be minor or solvable, because the developed formulas can be adapted to longer durations using the corresponding larger H_{\max} value.

The developed formulas can be conveniently applied to design practice if the commonly used wave parameters, viz., H_{\max} , H_s , and T_s are available. To predict H_{\max} and H_s in shallow and intermediate-depth waters from offshore waves, the Goda (1975) model may be applicable, which predicts the transformation of the wave height distribution due to shoaling and breaking, considering the variation in the sea level due to wave setdown and setup as well as surf beat. In the surf zone, H_{\max} can be approximated by a breaking-limited (or depth-limited) wave height, so that the existing breaker wave height formulas (reviewed by Rattanapitikon and Shibayama, 2000) may be available. However, because the data used to develop these formulas are mostly limited to measurements in intermediate-depth water ($1/20 < h/L < 1/2$), their applicability needs to be tested in shallow water ($h/L < 1/20$).

7. List of symbols

A	reference area of object
a_x, a_y, a_z	accelerations in x , y , and z axes
B_{50}	median surface grain size of seabed
C_F	maximum force coefficient
$C_F(K_C^*)$	C_F for maximum velocity waveform
D	reference width of object
D_{n50}	median nominal diameter of rocks defined as $(M_{50}/\rho_s)^{1/3}$
F_p	maximum or peak horizontal wave force
$F_{p,\max}$	highest maximum wave force in a random wave train
f_i	frequency of i -th Fourier component
f_{\min}	low cut-off frequency for wave motion
g	acceleration due to gravity
H^*	wave height at maximum velocity waveform
H_{m0}	significant wave height defined as four times the standard deviation of the surface elevation

H_s	significant wave height defined by zero down-crossing method
H_{\max}	maximum wave height
h	mean depth
K_C	Keulegan–Carpenter number
K_C^*	K_C for maximum velocity waveform
$K_{p\eta}(\omega_i)$	conversion factor from pressure to surface elevation for i -th Fourier component
$K_{pu}(\omega_i)$	conversion factor from pressure to velocity for i -th Fourier component
k_i	wave number for i -th Fourier component
k_s	wave number corresponding to T_s
L	wavelength corresponding to T_s
L_i	wavelength for i -th Fourier component
M_{50}	median mass of rocks
n	sample size
R_{adj}^2	adjusted R-squared
r_d	probability of significant move for isolated quarry rocks on a relatively flat bed
r_{pp}	ratio of $2T_{pp}^*$ to T_s
r_{zp}	ratio of $4U_{p+}^*T_{zp}^*$ to $U_{\text{Airy}}T_s$
SER	standard error of regression
s	bed slope
T_i	period of i -th Fourier component
T_{pp}	peak-to-peak period or period between successive negative and positive peak velocities
T_{pp}^*	T_{pp} of maximum velocity waveform
T_s	significant wave period defined by zero down-crossing method
T_{zp}	zero-to-peak period
T_{zp}^*	T_{zp} of maximum velocity waveform
t	time
U_{Airy}	reference velocity calculated from linear wave theory
U_a	velocity semi-amplitude
U_a^*	U_a of maximum velocity waveform
U_{p+}	positive peak velocities immediately after zero up-crossing
U_{p+}^*	U_{p+} of maximum velocity waveform
U_{p-}	negative peak velocity immediately before zero up-crossing
U_r	Ursel number defined as $H_{\max}L^2/h^3$
u_p	orbital velocity component in principal wave direction
u'_x, u'_y	cross-shore and longshore fluctuating velocities
z_p, z_u	vertical distances from seabed to pressure and velocity sensors
α	correction factor defined as U_a^*/U_{Airy}

$\alpha_{\text{lab}}, \alpha_{\text{field}}$	α from laboratory and field models
γ	change in relative direction of accelerometer
Δ	submerged specific density of rocks
θ_{50}	median friction angle in degrees
θ_p	principal wave direction
μ_{50}	median friction coefficient between rocks and seabed
ρ	mass density of fluid
ρ_s	mass density of rocks
ϕ	dimensionless predictor for r_d
ω_i	angular frequency of i -th Fourier component
ω_s	angular frequency defined as $2\pi/T_s$

Acknowledgments

We are grateful to N. Tanada for his assistance with the field studies off Tokushima. We would like to express our gratitude to N. Sugawara and other staff in the Fisheries Promotion Division of Hokkaido for their assistance with the field studies off Mashike. We would like to thank A. Watanuki and Y. Obata for the field measurements off Mashike. This study was conducted under the Fisheries Infrastructure Development Research Project supervised by the Japan Fisheries Agency.

Appendix A. Pressure-estimated vs. measured surface elevations and near-bed orbital velocities

The surface elevation data obtained by direct measurement using an ultrasonic wave gauge could be more accurate than those estimated from pressure. In high waves, however, the ultrasonic acoustic data were frequently missing or heavily contaminated with spikes, whereas the pressure data always appeared very reasonable without any apparent noise. Overall, the pressure-estimated surface elevations in moderately high waves demonstrated reasonable agreement with the acoustic measurements, despite slight underestimation of the crest height (Fig. A1). Because the pressure-estimated surface elevation has already been widely used to estimate the wave height and period in shallow and intermediate-depth waters, it was employed in this study as the most robust standard measure.

The near-bed wave orbital velocity is a two-dimensional (2D) vector quantity with directional spreading, and in nearshore areas it is affected by the reflected waves, whereas the pressure-estimated wave orbital velocity assumes that the directional spreading and reflection of the wave are negligible. However, 2D velocity signals obtained from ECMs were frequently contaminated with spikes in rough seas. Thus, the following validation was performed to ascertain the robustness and reliability of pressure-estimated wave orbital velocities to determine the single extreme value U_a^* in field environments. Firstly, velocity time-series data with any indication of actual velocities faster than the measurable limit (3 m/s) were removed from the analysis. Subsequently, the remaining sets of time-series data were demeaned and low-pass filtered with a cut-off frequency of 0.33 Hz to remove the fluctuations due to turbulence and noise. Secondly, to obtain the wave orbital velocity in the direction of wave propagation, the principal wave direction, θ_p , was defined as the direction corresponding to the maximum variance of the velocity components, i.e.,

$$\theta_p = \frac{1}{2} \arctan \frac{2\overline{u'_x u'_y}}{\overline{u'^2_x} - \overline{u'^2_y}}, \quad (\text{A1})$$

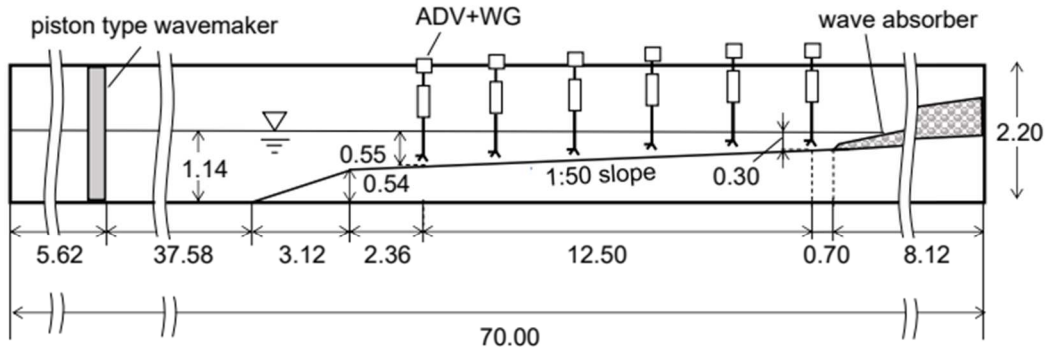
where θ_p is the angle between the wave incidence and shore normal; u'_x and u'_y are the cross-shore and longshore fluctuating velocities, respectively; and the overline represents the average during each burst. Finally, the orbital velocity component in the principal wave direction, denoted by u_p , was compared to the pressure-estimated orbital velocities. Despite periodically increasing deviation from u_p during a burst (Fig. A2), the U_a^* value obtained from the pressure-estimated orbital velocities showed overall good agreement with that calculated from u_p (Fig. A3), indicating that the pressure-estimated U_a^* value can also be used as a robust and reliable estimate of U_a^* .

References

- Denny, M., 1995. Predicting physical disturbance: mechanistic approaches to the study of survivorship on wave-swept shores. *Ecol. Monogr.* 65, 371–418. <https://doi.org/10.2307/2963496>.
- Dibajnia, M., Moriya, T., Watanabe, A., 2001. A representative wave model for estimation of nearshore local transport rate. *Coast. Eng. J.* 43, 1–38. <https://doi.org/10.1142/S0578563401000256>.
- Elfrink, B., Hanes, D.M., Ruessink, B.G., 2006. Parameterization and simulation of near bed orbital velocities under irregular waves in shallow water. *Coast. Eng.* 53, 915–927. <https://doi.org/10.1016/j.coastaleng.2006.06.002>.
- Goda, Y., 1975. Irregular wave deformation in the surf zone. *Coast. Eng. Jpn.* 18, 13–26. <https://doi.org/10.1080/05785634.1975.11924196>.
- Goda, Y., 1988. Statistical variability of sea state parameters as a function of wave spectrum. *Coast. Eng. Jpn.* 31, 39–52. <https://doi.org/10.1080/05785634.1988.11924482>.
- Gudmestad, O.T., 1993. Measured and predicted deep water wave kinematics in regular and irregular seas. *Mar. Struct.* 6, 1–73. [https://doi.org/10.1016/0951-8339\(93\)90009-R](https://doi.org/10.1016/0951-8339(93)90009-R).
- ISO 21650, 2007. Actions from Waves and Currents on Coastal Structures. International Standard, 1st ed., 2007-10-15.
- Kawamata, S., Kobayashi, M., 2022. Modified formula for predicting the maximum wave force on seabed objects. *Ocean. Eng.* 266, 112751. <https://doi.org/10.1016/j.oceaneng.2022.112751>.
- Kawamata, S., Kobayashi, M., Tanada, N., 2018. Empirical model for probabilistic rock stability on flat beds under waves with or without currents. *Coast. Eng.* 140, 257–271. <https://doi.org/10.1016/j.coastaleng.2018.08.005>.
- Lorang, M.S., 2000. Predicting threshold entrainment mass for a boulder beach. *J. Coast. Res.* 16, 432–445. <https://www.jstor.org/stable/4300052>.
- Nott, J., 1997. Extremely high-energy wave deposits inside the Great Barrier Reef, Australia: determining the cause—tsunami or tropical cyclone. *Mar. Geol.* 141, 193–207. [https://doi.org/10.1016/S0025-3227\(97\)00063-7](https://doi.org/10.1016/S0025-3227(97)00063-7).
- Rattanapitikon, W., Shibayama, T., 2000. Verification and modification of breaker height formulas. *Coast. Eng. J.* 42, 389–406. <https://doi.org/10.1142/S0578563400000195>.
- Sarpkaya, T., Isaacson, M., 1981. *Mechanics of Wave Forces on Offshore Structures*. Van Nostrand Reinhold Co., New York.
- Sobey, R.J., 1990. Wave theory predictions of crest kinematics, in: Tørum, A., Gudmestad, O.T. (Eds.), *Water Wave Kinematics*. Kluwer Academic Publishers, pp. 215–231.
- Soulsby, R.L., 1987. Calculating bottom orbital velocity beneath waves. *Coast. Eng.* 11, 371–380. [https://doi.org/10.1016/0378-3839\(87\)90034-2](https://doi.org/10.1016/0378-3839(87)90034-2).

- Tajima, Y., 2004. Waves, currents, and sediment transport in the surf zone along long, straight beaches. PhD thesis, Massachusetts Institute of Technology, Cambridge, MA.
- Tajima, Y., Madsen, O.S., 2002. Shoaling, breaking and broken wave characteristics. Proceedings of the 28th International Conference on Coastal Engineering. World Scientific, pp. 222–234. https://doi.org/10.1142/9789812791306_0020.
- Wiberg, P.L., Sherwood, C.R., 2008. Calculating wave-generated bottom orbital velocities from surface-wave parameters. *Comput. Geosci.* 34, 1243–1262. <https://doi.org/10.1016/j.cageo.2008.02.010>.

A. Wave flume with 1:50 slope



B. Wave flume with 1:30 slope

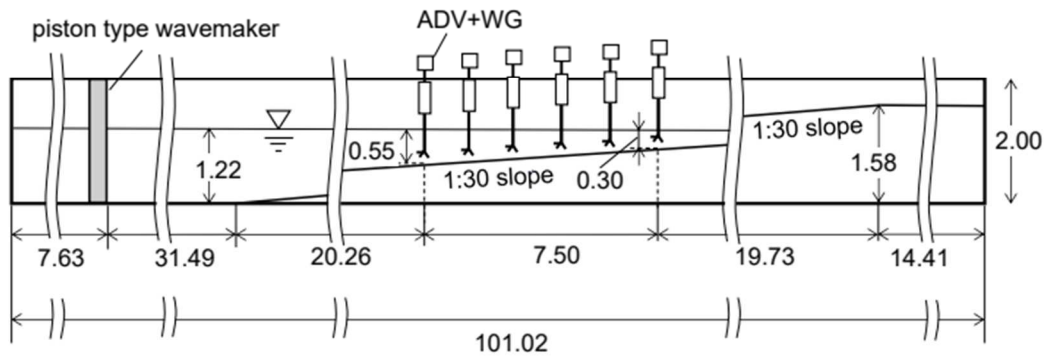


Fig. 1. Wave flume dimensions (unit: m) and locations of measurement instruments. Acoustic Doppler velocimeters (ADV) and wave gauges (WG) were installed at six measurement points on the slope at different depths.

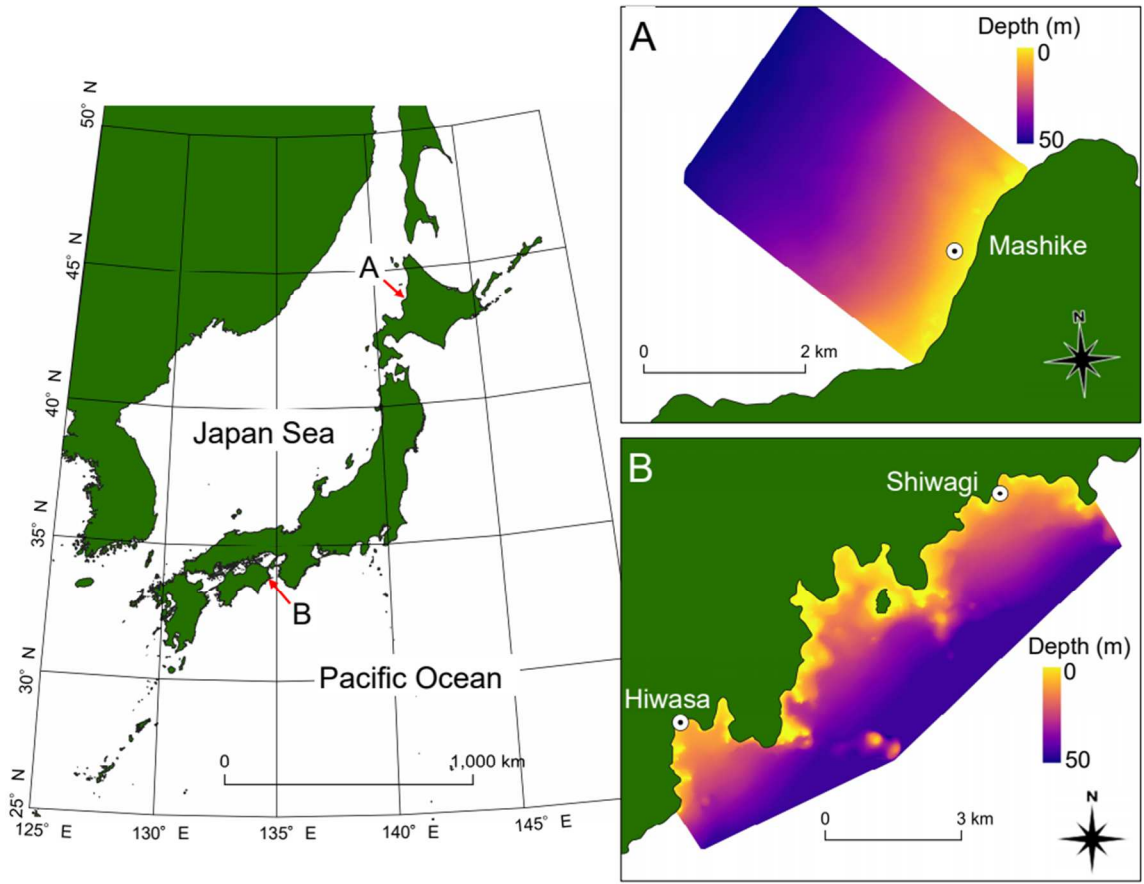


Fig. 2. Map of field locations (circled dots) and bathymetry of the surrounding areas.

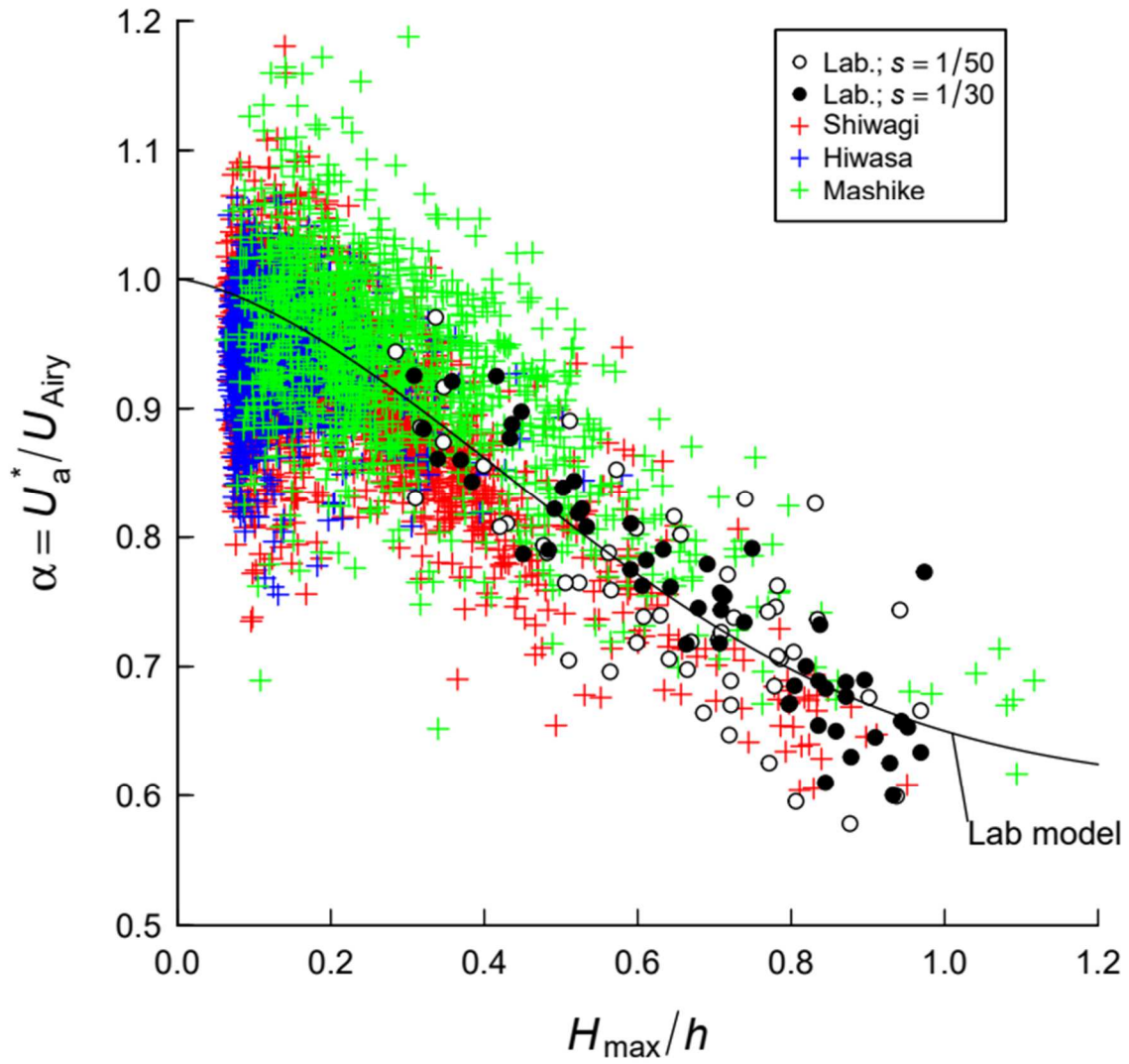


Fig. 3. Variation in $\alpha \equiv U_a^*/U_{\text{Airy}}$ with H_{\max}/h . s : bed slope. The solid curve indicates the laboratory model of Eq. (12).

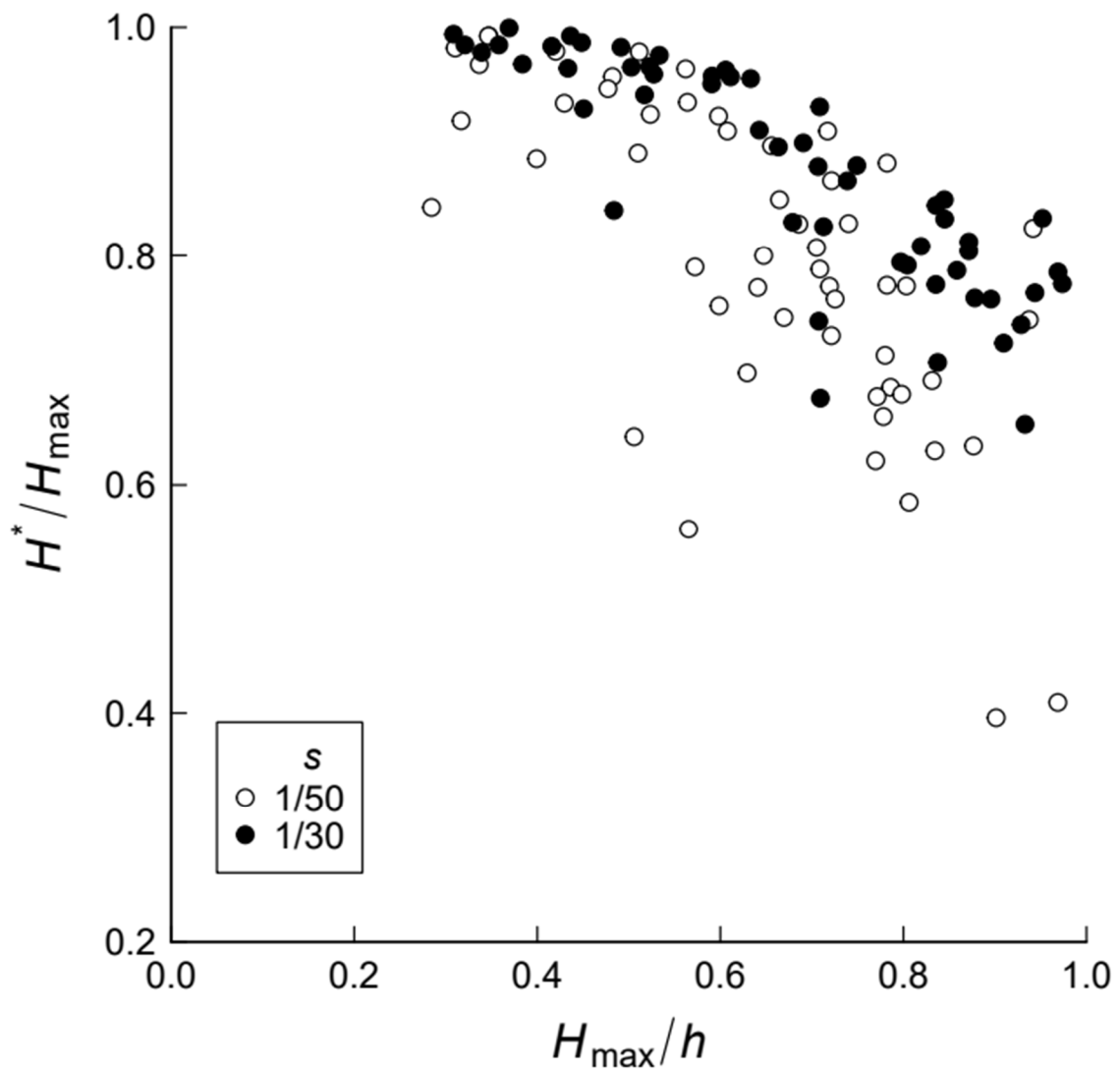


Fig. 4. Variation in the ratio of the wave height at the maximum velocity waveform to the maximum wave height, H^*/H_{\max} , with H_{\max}/h . Only data obtained from laboratory experiments are shown.

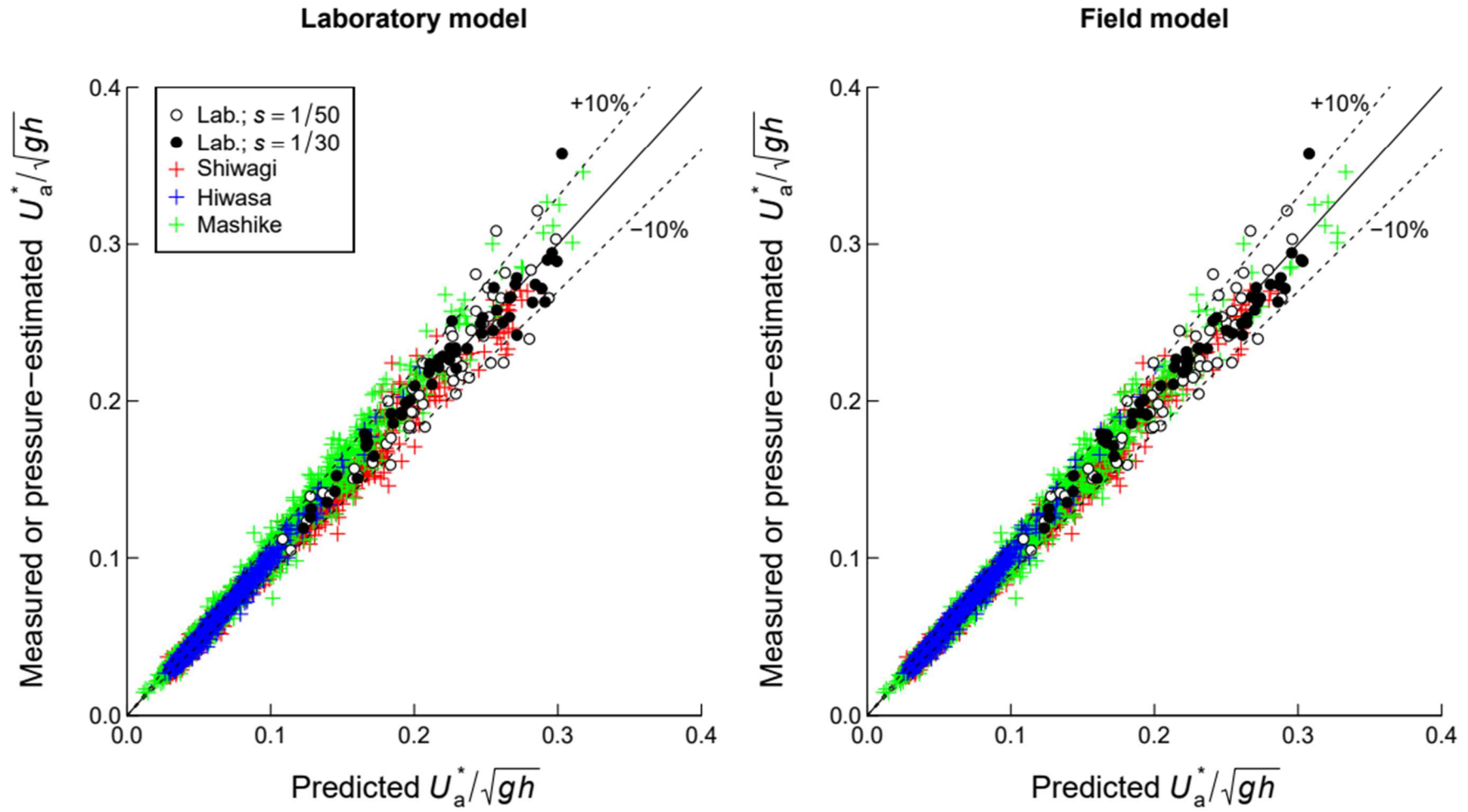


Fig. 5. Comparison of U_a^* predictions from laboratory (left; Eq. (12)) and field models (right; Eq. (13)) versus measured (in laboratory) or pressure-estimated (in field) U_a^* .

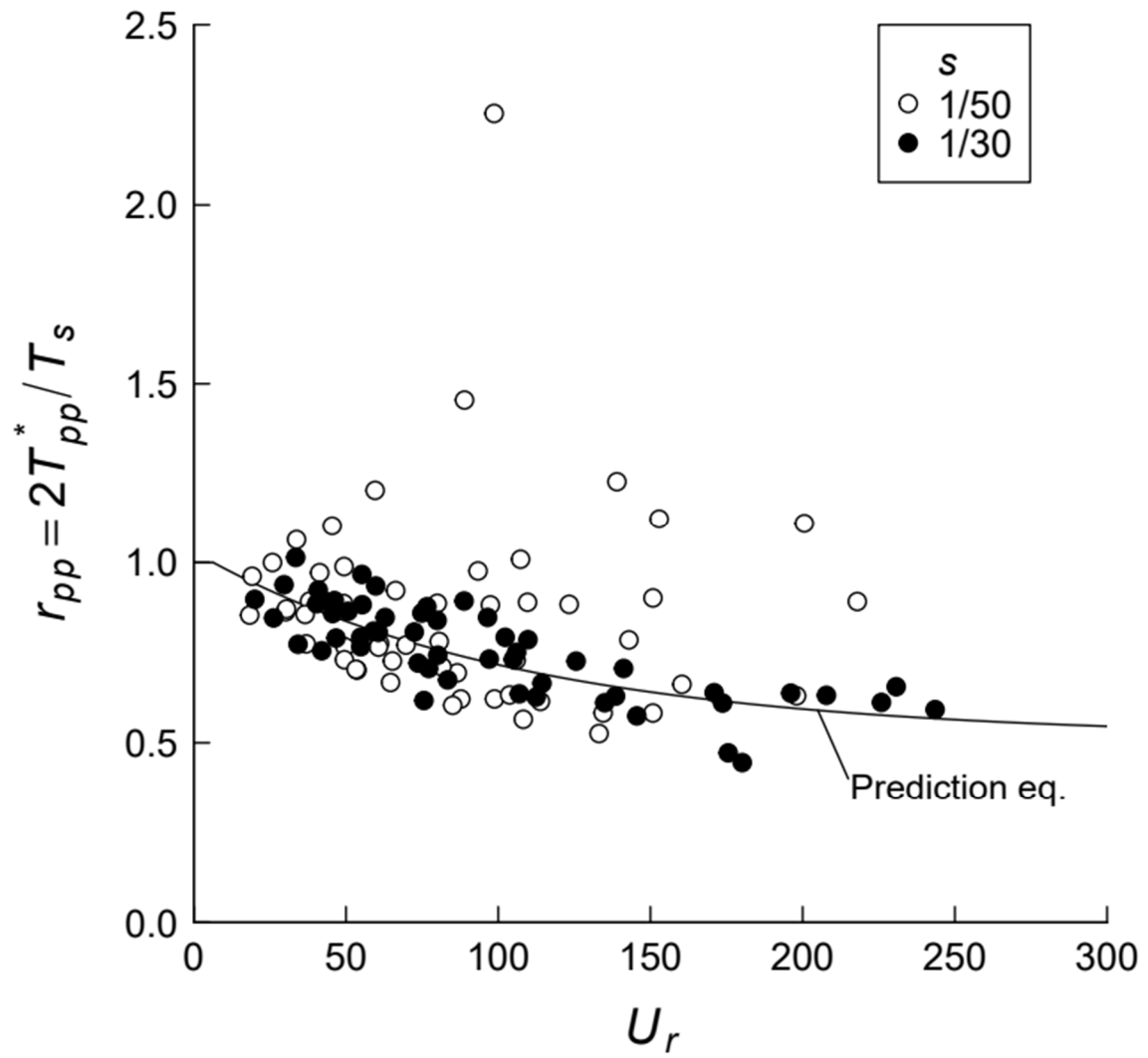


Fig. 6. Variations in r_{pp} with U_r . The solid curve corresponds to Eq. (14).

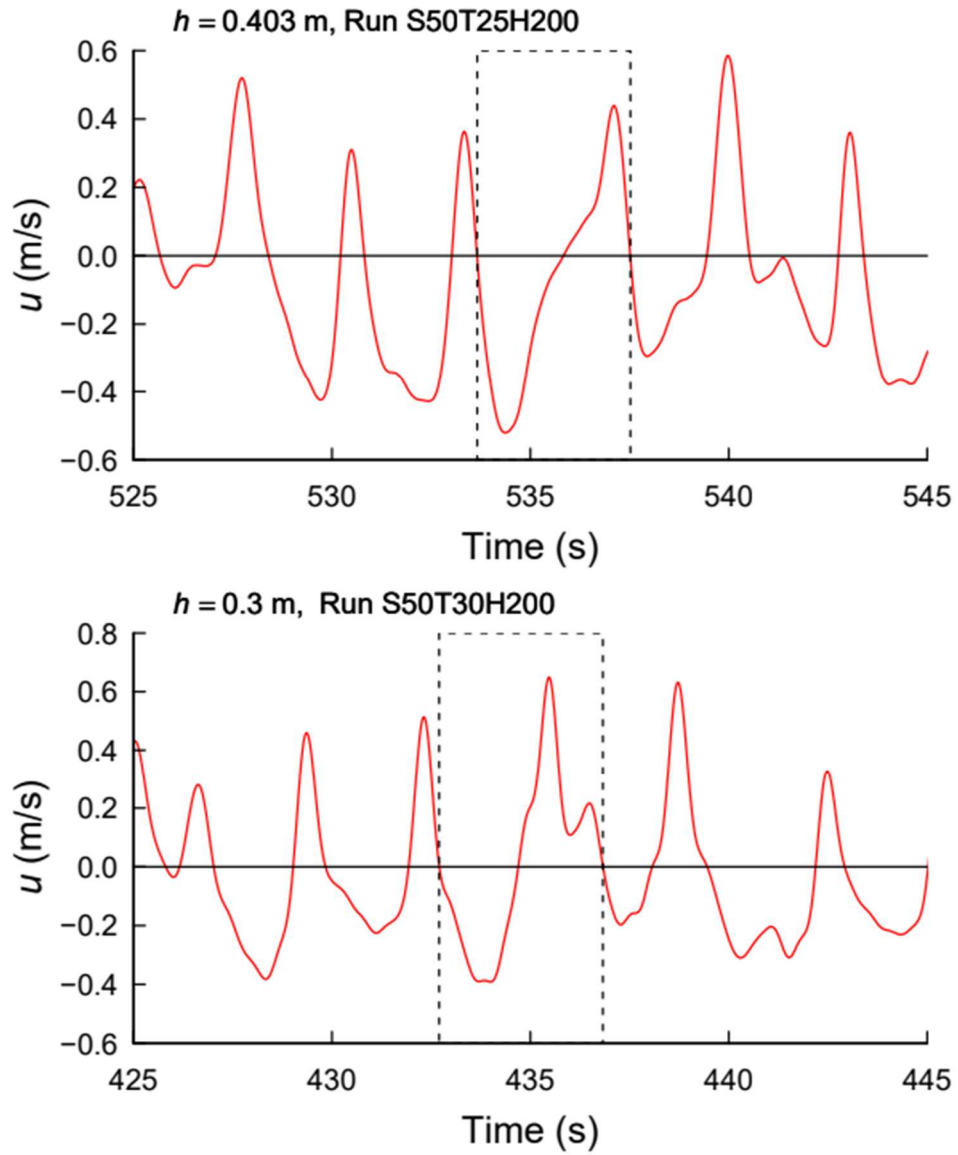


Fig. 7. Examples of maximum velocity waveforms with unexpectedly large r_{pp} values. The velocity waveforms in dashed-line rectangles are the maximum velocity waveforms.

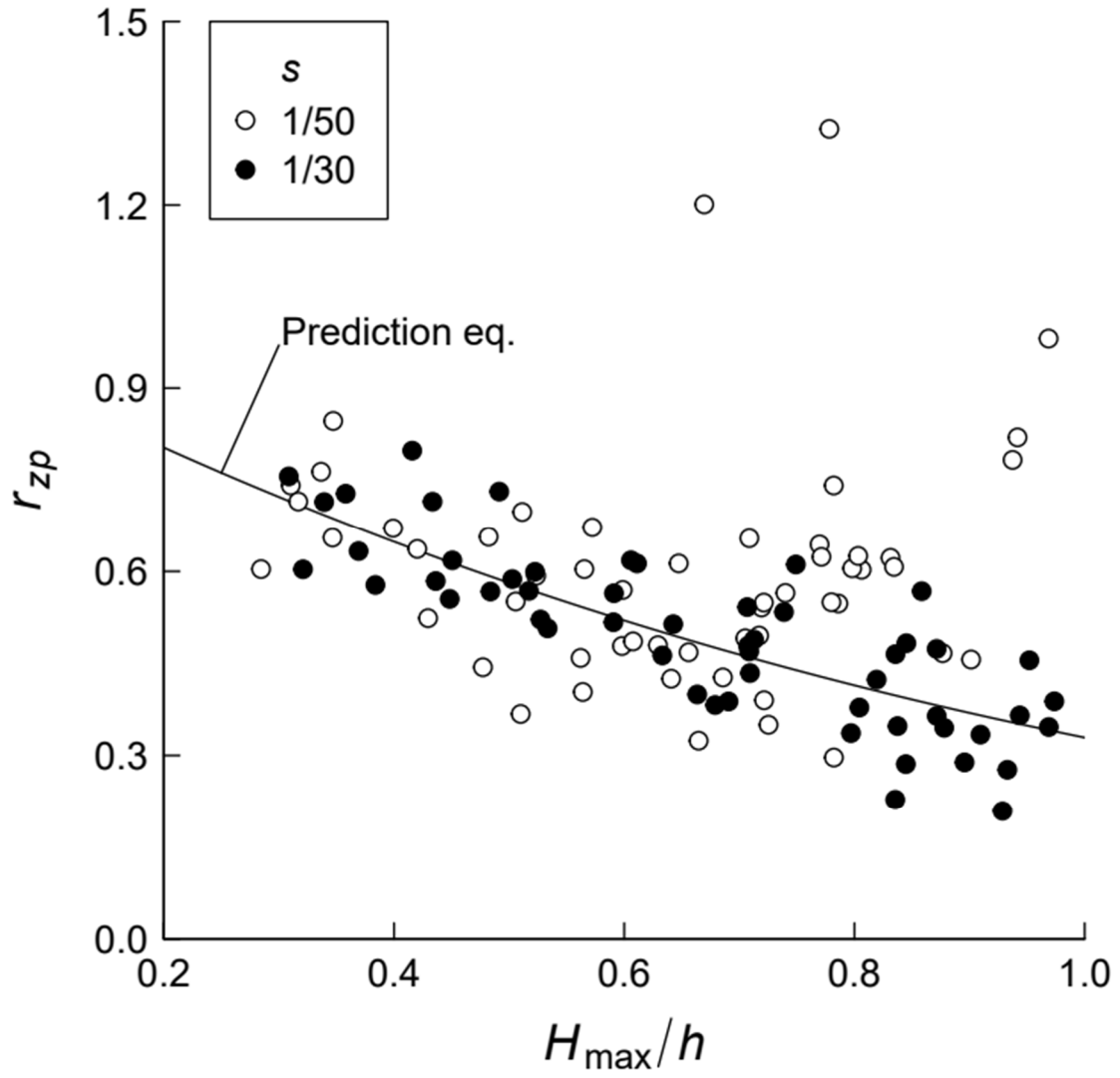


Fig. 8. Variations in r_{zp} with H_{\max}/h . The solid curve corresponds to Eq. (15).

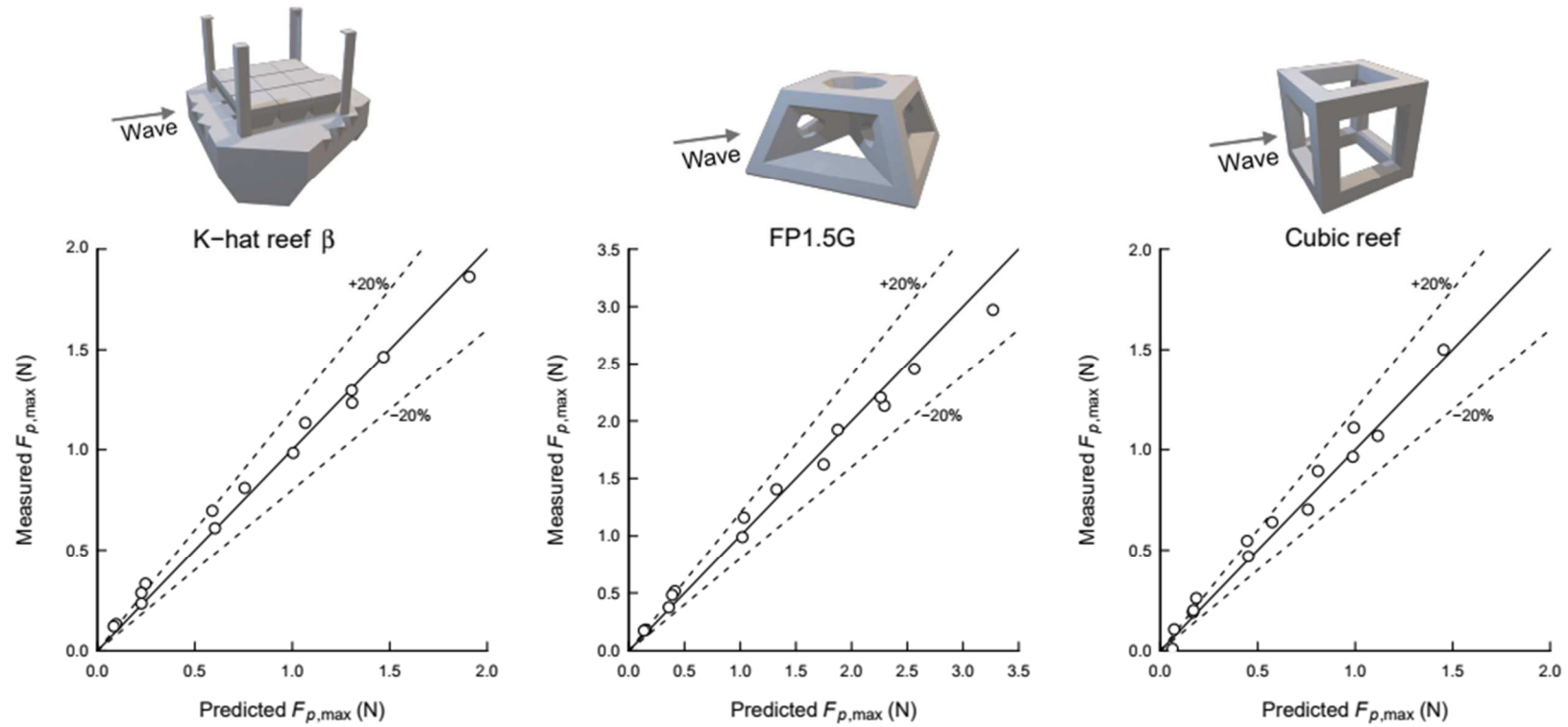


Fig. 9. Comparison between predicted and measured $F_{p,max}$ on three artificial reef models under random waves. Data are from the experimental study of Kawamata and Kobayashi (2022).

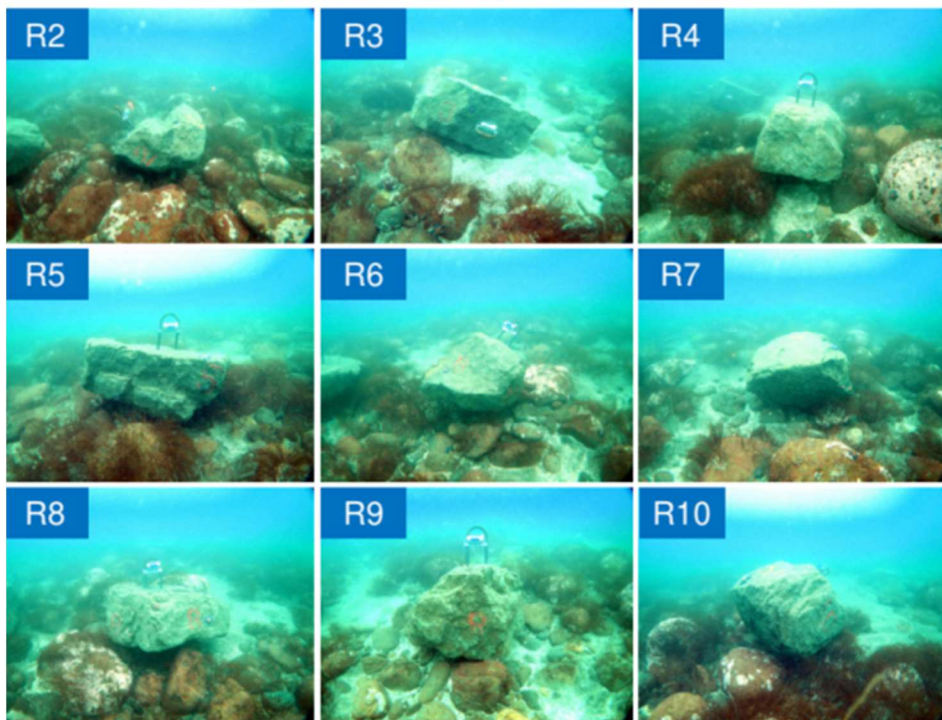
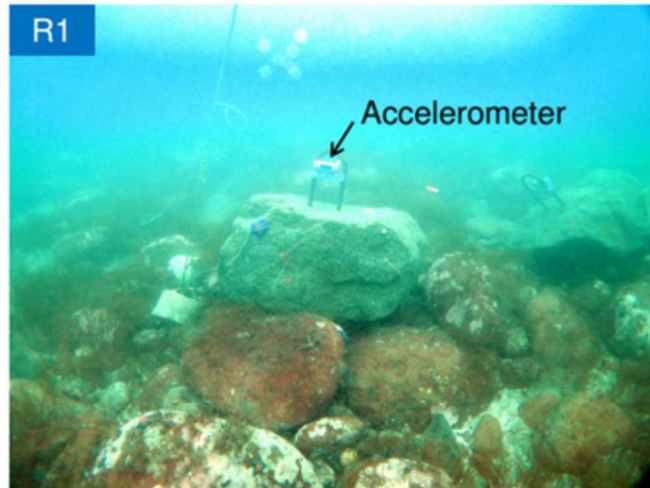


Fig. 10. Ten quarry rocks with accelerometers placed at the test site off Mashik

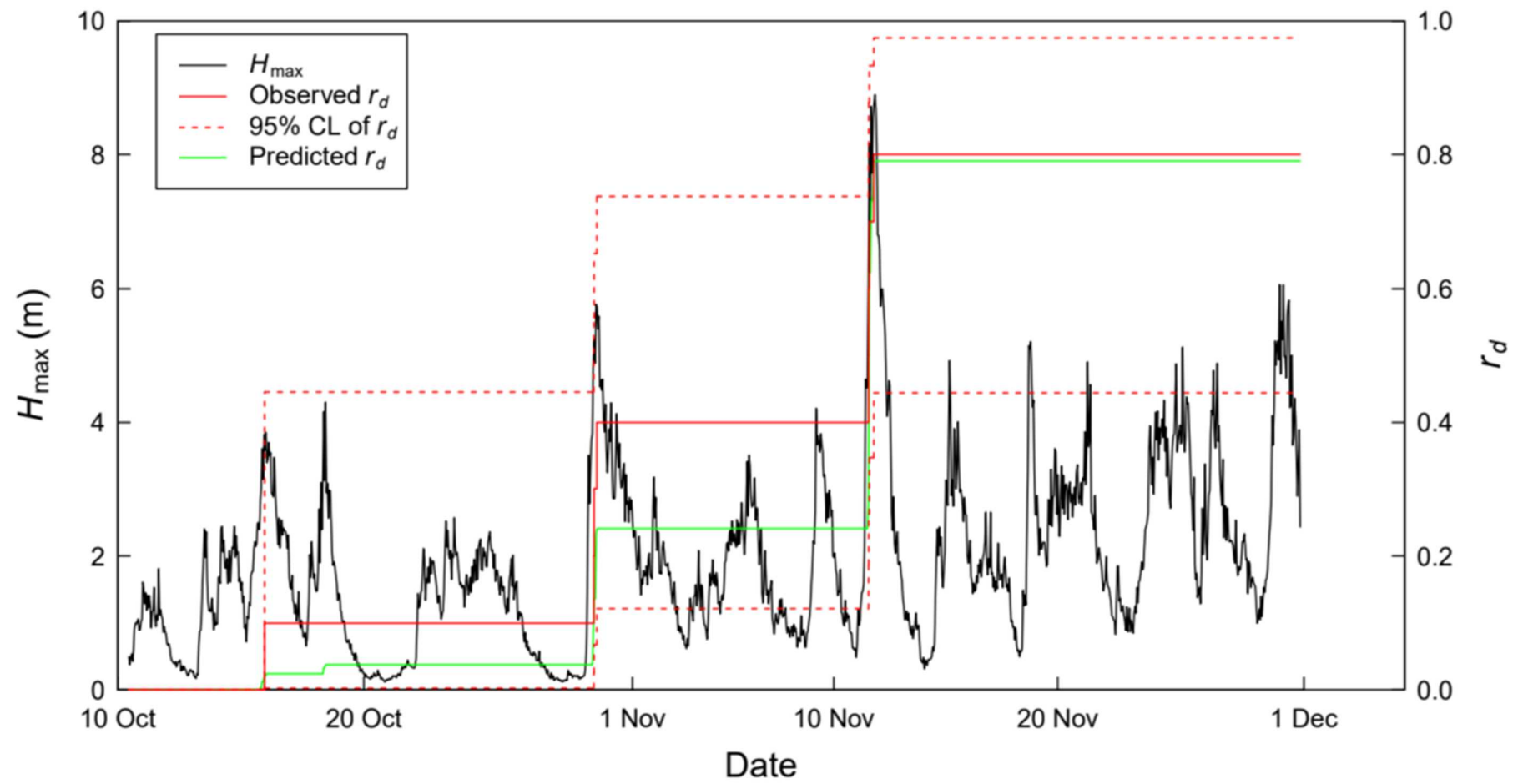


Fig. 11. Temporal variations in H_{\max} , and the observed and predicted movement ratios, r_d , of quarry rocks in field test.

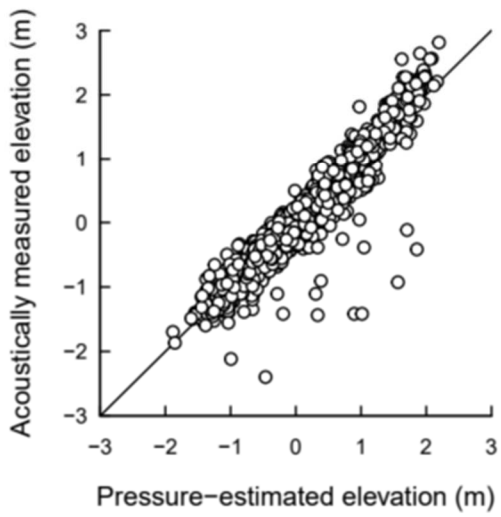
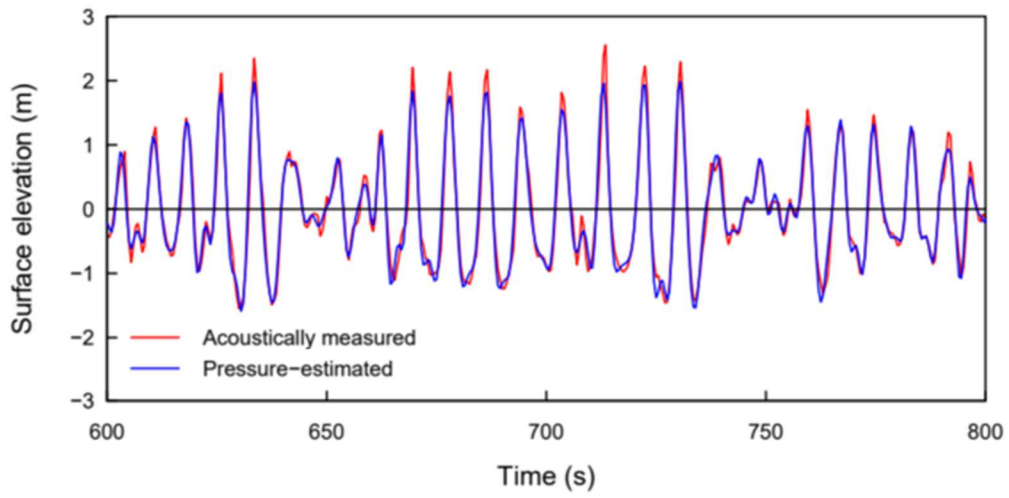


Fig. A1. Example of the comparison between the pressure-estimated and acoustically measured surface elevations. Data obtained during a burst measurement period of 20 min are shown only partially in time series (upper) but all in scatter plot form (lower).

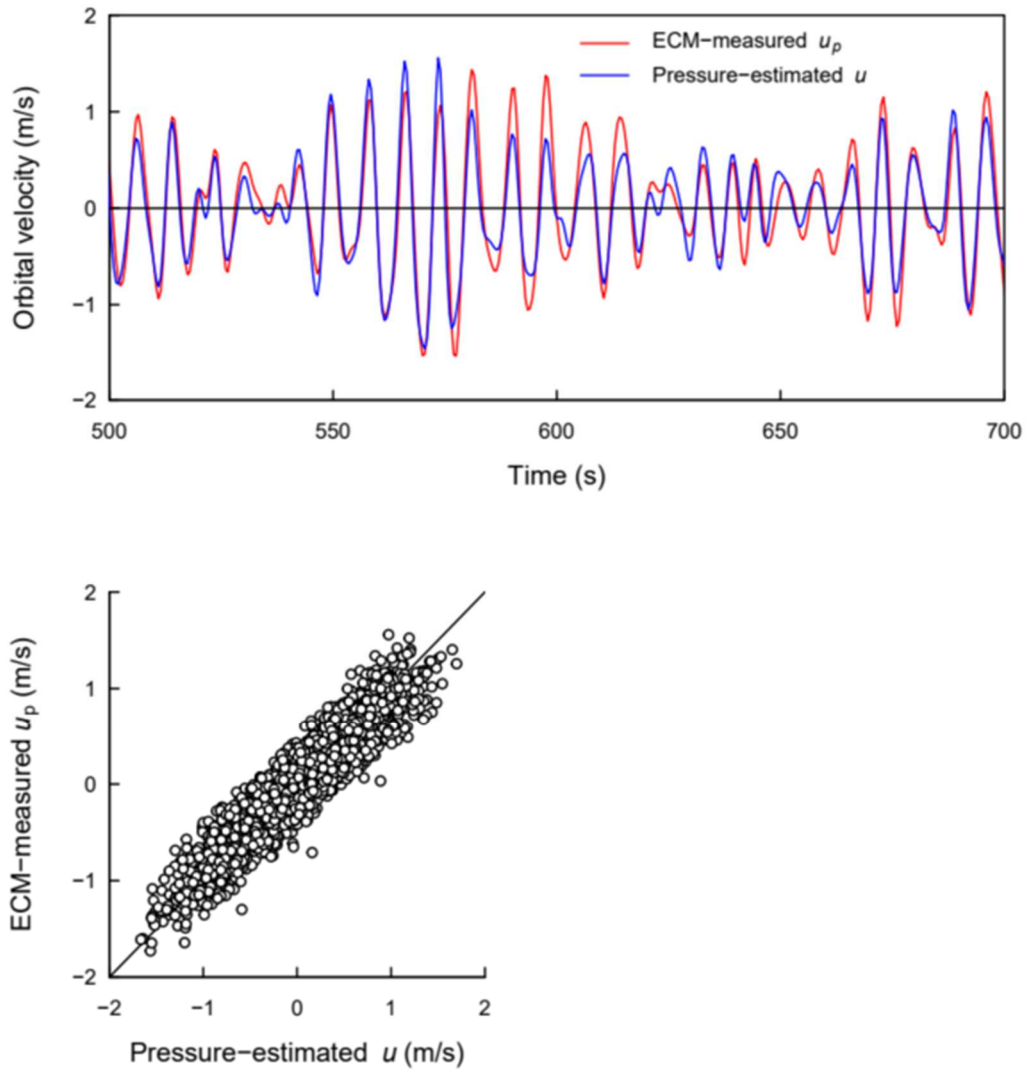


Fig. A2. Example of the comparison between the pressure-estimated orbital velocities and ECM-measured orbital velocity components in the principal wave direction, u_p . Data obtained during a burst measurement period of 20 min are shown only partially in time series (upper) but all in scatter plot form (lower).

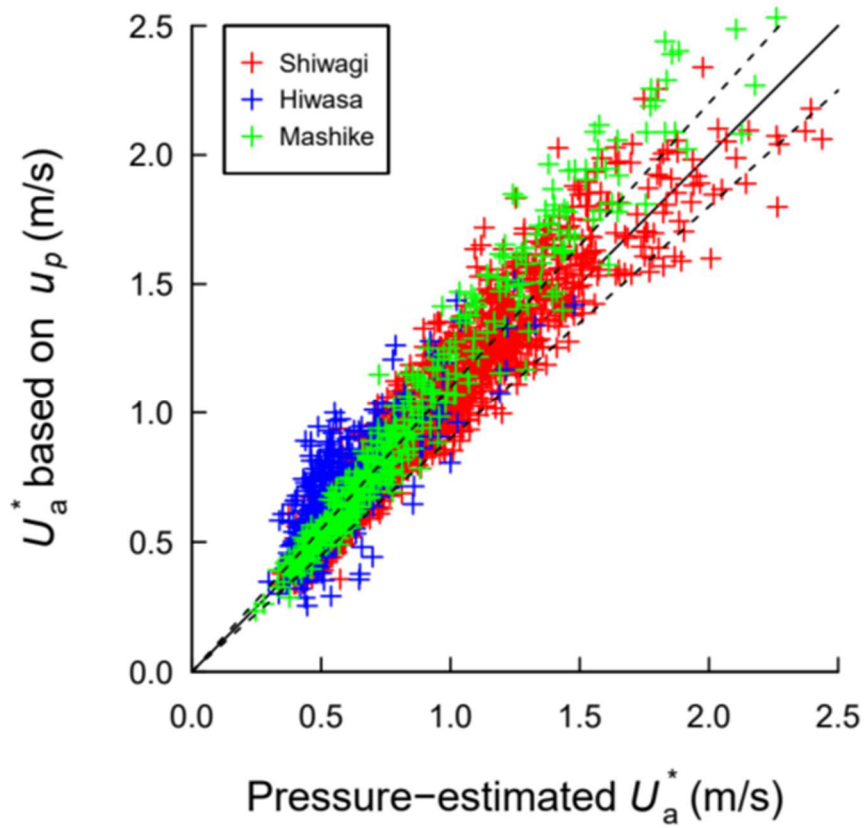


Fig. A3. Comparison between pressure-estimated U_a^* and U_a^* based on ECM-measured u_p . The solid line indicates perfect agreement between them, and the upper and lower broken lines represent $\pm 20\%$ error limits.

Table 1

Experimental conditions for laboratory measurements of near-bed wave orbital velocity and surface elevation

Run	s	$H_{s,0}$ ^a (m)	$T_{s,0}$ ^b (s)	No. of waves	Wave conditions at measurement depths		
					h/L ^c	H_s/h	H_{\max}/h
S50T20H100	1/50	0.100	1.98	367–416	0.092–0.130	0.172–0.320	0.284–0.565
S50T20H150	1/50	0.151	1.98	359–407	0.092–0.132	0.266–0.487	0.506–0.786
S50T20H200	1/50	0.201	2.01	359–384	0.092–0.130	0.365–0.593	0.629–0.831
S50T25H100	1/50	0.100	2.54	308–350	0.078–0.102	0.186–0.344	0.317–0.647
S50T25H150	1/50	0.149	2.51	312–353	0.082–0.102	0.288–0.513	0.511–0.834
S50T25H200	1/50	0.200	2.53	313–332	0.082–0.105	0.403–0.646	0.717–0.942
S50T30H100	1/50	0.101	3.04	274–308	0.067–0.081	0.204–0.416	0.347–0.770
S50T30H150	1/50	0.148	3.03	274–299	0.067–0.081	0.316–0.579	0.562–0.901
S50T30H200	1/50	0.198	3.06	261–296	0.066–0.084	0.438–0.638	0.725–0.969
S30T20H100	1/30	0.112	2.00	340–353	0.094–0.130	0.188–0.395	0.339–0.679
S30T20H150	1/30	0.176	2.02	339–353	0.093–0.130	0.297–0.620	0.503–0.836
S30T20H200	1/30	0.233	2.03	329–344	0.090–0.130	0.406–0.702	0.691–0.896
S30T25H100	1/30	0.116	2.54	280–289	0.070–0.098	0.209–0.468	0.321–0.845
S30T25H150	1/30	0.162	2.56	273–286	0.072–0.099	0.295–0.674	0.448–0.929
S30T25H200	1/30	0.208	2.48	275–297	0.074–0.103	0.388–0.764	0.591–0.952
S30T30H100	1/30	0.119	3.08	235–250	0.062–0.081	0.226–0.546	0.309–0.878
S30T30H150	1/30	0.161	2.97	242–258	0.064–0.085	0.308–0.723	0.433–0.944
S30T30H200	1/30	0.214	3.00	242–251	0.063–0.085	0.422–0.820	0.606–0.974

^a $H_{s,0}$: incident offshore significant wave height.

^b $T_{s,0}$: incident offshore significant wave period.

^c L : wavelength corresponding to the significant wave period.

Table 2

Summary of wave field measurements

Location name	Latitude and longitude	Measurement period	h (m)	Mean slope	No. of waves ^a	h/L ^b	H_s/L	H_{\max}/h
Shiwagi	33°46.95'N, 134°37.21'E	29 July–17 Nov. 2015	7.7–10.5	0.033	88–259	0.065–0.290	0.0036–0.056	0.063–0.951
Hiwasa	33°44.19'N, 134°32.66'E	22 Nov. 2018– 5 Feb. 2019	3.9–6.1	0.060	120–282	0.046–0.184	0.0023–0.0351	0.063–0.579
Mashike	43°50.91'N, 141°30.03'E	9 Oct.–30 Nov. 2017	7.1–8.3	0.019	123–339	0.084–0.379	0.0069–0.0880	0.063–1.117

^a Number of zero-down-crossing waves during a burst.

^b L : wavelength corresponding to the significant wave period.

Table 3

Standardized partial regression coefficients from a multiple regression of relative error $U_a^*/(\alpha_{\text{lab}}U_{\text{Airy}})$ on possible parameters other than H_{max}/h . The regressions were performed using field data ($n = 4005$) of $H_{m0} > 0.4$ m. The parameters are presented in descending order of magnitude.

Parameter	Standardized partial regression coefficient
H_s/L	2.167
$\sqrt{h/g}/T_s$	-1.482
h/L	1.196
H_s/h	-0.900
H_{max}/L	-0.886